arXiv:astro-ph/9905343v1 26 May 1999

GHRS and ORFEUS-II Observations of the Highly Ionized Interstellar Medium Toward ESO 141-055[1]

Kenneth R. Sembach
Department of Physics & Astronomy, The Johns Hopkins University, 3400 N. Charles St., Baltimore, MD 21218
sembach@pha.jhu.edu

Blair D. Savage
Department of Astronomy, University of Wisconsin - Madison, 475 N. Charter St., Madison, WI 53706
savage@astro.wisc.edu

Mark Hurwitz
Space Sciences Laboratory, University of California, Berkeley, CA 94720
markh@ssl.berkeley.edu

ABSTRACT

We present Goddard High Resolution Spectrograph and ORFEUS-II measurements of Si IV, C IV, N V, and O VI absorption in the interstellar medium of the Galactic disk and halo toward the nucleus of the Seyfert galaxy ESO 141-055. The high ionization absorption is strong, with line strengths consistent with the spectral signature expected for hot ($T \gtrsim 10^5$ K) collisionally ionized gas in either a "Galactic fountain" or an inhomogeneous medium containing a mixture of conductive interfaces and turbulent mixing layers. The total O VI column density of $\approx 10^{15}$ cm^{-2} suggests that the scale height of O VI is large ($\gtrsim$3 kpc) in this direction. Models of the C IV velocity distribution along the sight line are consistent with a large scale height for the highly ionized gas. Comparison of the high ion column densities with measurements for other sight lines indicates that the highly ionized gas distribution is patchy. The amount of O VI perpendicular to the Galactic plane varies by at least a factor of ~ 4 among the complete halo sight lines thus far studied. In addition to the high

[1]Based on observations with the NASA/ESA Hubble Space Telescope, obtained at the Space Telescope Science Institute, which is operated by the Association of Universities for Research in Astronomy, Inc. under NASA contract NAS5-26555.

ion absorption, lines of low ionization species are also present in the spectra. With the possible exception of Ar I, which may have a lower than expected abundance resulting from partial photoionization of gas along the sight line, the absorption strengths are typical of those expected for the warm, neutral interstellar medium. The sight line intercepts a cold molecular cloud with $N(H_2) \approx 10^{19}$ cm^{-2}. The cloud has an identifiable counterpart in IRAS 100μm emission maps of this region of the sky. We detect a Lyα absorber associated with ESO 141-055 at $z = 0.03492$. This study presents an enticing glimpse into the interstellar and intergalactic absorption patterns that will be observed at high spectral resolution by the Far Ultraviolet Spectroscopic Explorer.

Subject headings: galaxies: individual (ESO 141-055) – Galaxy: halo – galaxies: absorption lines – ISM: abundances – ISM: clouds – ISM: molecules – ultraviolet: ISM

1. Introduction

The distribution of highly ionized gas in the Galaxy contains information about the physical processes that transport gas and energy within the interstellar medium and intergalactic medium. Absorption line observations of highly ionized atoms (e.g., Si IV, C IV, N V, O VI) toward extragalactic continuum sources are particularly valuable since the interstellar medium (ISM) along entire paths through the Galaxy can be sampled and the total velocity extents and column densities of the absorption measured. These quantities provide important benchmarks for comparisons with observations of the disks and halos of other galaxies detected through their absorption line signatures against distant quasars (Steidel 1990; Lu et al. 1995; Burles & Tytler 1996; Songaila & Cowie 1996; Savage, Tripp, & Lu 1998). They also provide impetus for theoretical models describing the distribution and ionization of gas in galaxies (Spitzer 1990) and in the intergalactic medium (Cen & Ostriker 1999).

Savage, Sembach, & Lu (1997) have recently summarized most of the available Galactic high ion (Si IV, C IV, and N V) data obtained with the Goddard High Resolution Spectrograph (GHRS) aboard the Hubble Space Telescope (HST). The high ion species have large scale heights perpendicular to the Galactic plane ($h_z \sim 3-5$ kpc) and ionic ratios that are suggestive of multiple, collisionally ionized regions with temperatures of $\sim 10^5$ K. The highly ionized gas distribution is patchy and dependent upon the types of large scale interstellar structures encountered (Sembach, Savage, & Tripp 1997). High quality C IV and

N V absorption line data is available for approximately one dozen complete paths through the Galactic halo, but information for Si IV exists for only a few such sight lines (3C 273, Mrk 509, and a few stars in the Large and Small Magellanic Clouds). This situation will improve rapidly in the near future as extragalactic objects are observed with the Space Telescope Imaging Spectrograph (STIS) aboard the HST.

Information about O VI absorption in the Galactic halo is also scarce. Observations of O VI toward extragalactic sources are limited to data collected with the Hopkins Ultraviolet Telescope (HUT) and the Orbiting and Retrievable Far and Extreme Ultraviolet Spectrometers (ORFEUS) flown on two Space Shuttle missions. Widmann et al. (1998) recently reported an O VI scale height of $5.50\pm^{2.37}_{2.09}$ kpc based upon moderate resolution ($\sim$0.2Å) ORFEUS-II echelle spectrometer observations of one SMC star (HD 5980) and several LMC stars (HD 36402, HD 269546, LH 10:3120, and Sk –67 166). ORFEUS-I and II data obtained with the Berkeley Spectrograph for the sight lines to 3C 273 (Hurwitz et al. 1998a) and NGC 346 and PKS 2155-304 (Hurwitz et al. 1995) are marginally consistent with this result. Eventually, the Far Ultraviolet Spectroscopic Explorer (FUSE) will provide high-resolution O VI observations toward AGNs and QSOs, but until then halo gas studies are limited to lower resolution data that provide reliable measures of the total amount of O VI but do not allow for detailed velocity comparisons with the existing C IV and N V data.

Obtaining complete sets of high ion column density measurements toward AGNs and QSOs has been a primary observational limitation to understanding the highly ionized ISM in the Galactic halo. This information is necessary input for theories seeking to describe the production, distribution, and non-equilibrium cooling of hot (10^5–10^6 K) gas in the halo. Currently, a complete set of high ion measurements exists only for the 3C 273 sight line. The present study provides information for the high ionization lines of Si IV $\lambda\lambda$1393.76, 1402.77, C IV $\lambda\lambda$1548.19, 1550.77, N V $\lambda\lambda$1238.82, 1242.80, and O VI $\lambda\lambda$1031.93, 1037.62 toward ESO 141-055 ($l = 338.18°$, $b = -26.71°$). ESO 141-055 is classified in the NASA/IPAC Extragalactic Database as a Seyfert 1 galaxy at a redshift of 0.0371±0.0003 (de Vaucouleurs et al. 1991). It is bright enough at ultraviolet (UV) wavelengths to be observed with existing instrumentation in reasonable exposure times ($f_{UV} \sim 10^{-14} - 10^{-13}$ erg cm^{-2} s^{-1} Å^{-1}).

This study is organized as follows. In §2 we describe the observations and data reduction. Section 3 contains the basic measurements for the GHRS and ORFEUS-II data. We analyze the properties of the high ionization gas in §4, the low ionization gas in §5, and the molecular gas along the sight line in §6. We provide a short summary of our conclusions in §7.

2. Observations and Reductions

2.1. Goddard High Resolution Spectrograph Data

We used the GHRS on the HST to obtain intermediate-resolution spectra of the Si IV (1381.8–1418.6 Å), C IV (1519.8–1556.1 Å), and N V (1228.7–1265.9 Å) spectral regions of ESO 141-055 in October 1996 as part of HST Guest Observer program GO-6451. The galaxy was centered in the large ($1\farcs74\times1\farcs74$) science aperture and observed with the G160M first-order grating. Integration times were 9185 seconds for Si IV, 10423 seconds for C IV, and 9177 seconds for N V. We used standard carrousel rotation (FP-Split) and spectrum deflection procedures to reduce fixed-pattern noise caused by irregularities in the detector window and photocathode response. We used detector substepping pattern #5 to provide full-diode array observations of the interorder backgrounds, which we subtracted from the extracted spectra. The extracted spectra contained four substeps per resolution element (1 diode), which we rebinned to two samples per resolution element to improve the signal-to-noise ratio without significant loss of spectral resolution. Approximate S/N levels of 13, 11, and 21 per resolution element were achieved for the Si IV, C IV, and N V spectral regions, respectively.

We co-added the individual FP-Split sub-exposures using the nominal pixel offsets determined from the grating carrousel rotation since the signal of the individual sub-exposures was insufficient to centroid accurately on the interstellar profiles. There were 24 sub-exposures for the Si IV and N V spectral regions and 28 (16+12) sub-exposures for the C IV spectral region. These post-COSTAR[2] observations have a Gaussian core containing $\approx 70\%$ of the light and a broad wing containing $\approx 30\%$ of the light (see Figure 4 of Robinson et al. 1998). The spectral resolution (FHWM) is approximately 14 $\mathrm{km\,s^{-1}}$ at 1550 Å, 16 $\mathrm{km\,s^{-1}}$ at 1400 Å, and 18 $\mathrm{km\,s^{-1}}$ at 1250 Å.

The wavelength accuracy of the observations is approximately ±1 diode (1σ), which corresponds to 18–14 $\mathrm{km\,s^{-1}}$ over the 1250–1550 Å wavelength range. All velocities have been referenced to the Local Standard of Rest defined by Mihalas & Binney (1981)[3], where $v_{\mathrm{LSR}} = v_{\mathrm{HELIO}} + 0.4$ $\mathrm{km\,s^{-1}}$ for the ESO 141-055 sight line.

The fully reduced GHRS data are displayed in Figure 1. The 1σ error spectra are shown below each data spectrum. Interstellar lines discussed later are labeled. The data are

[2]COSTAR is the Corrective Optics Space Telescope Axial Replacement used to correct the spherical aberration in the HST primary mirror.

[3]Their reduction to the LSR assigns a solar speed of 16.5 $\mathrm{km\,s^{-1}}$ in the direction $l = 53°$, $b = +25°$.

preserved in the HST archive with identifications of Z3170105T (Si IV), Z317010BT/DT (C IV), and Z3170105T (N V). Additional information about the in-orbit performance of the GHRS can be found in articles by Brandt et al. (1994) and Heap et al. (1995). Technical information about the instrument can be found in Soderblom et al. (1994).

2.2. ORFEUS-II Data

We observed ESO 141-055 with the Berkeley spectrograph aboard the ORFEUS telescope during the ORFEUS-Shuttle Pallet Satellite (SPAS) II mission in November 1996. The exposure time for the observation was 13828 seconds, the longest of the mission. Background levels were monitored in an adjacent off-axis slit and were subtracted from the on-source data. We produced an extracted, calibrated, airglow-cleaned spectrum using the standard reduction procedures and calibration files available at the University of California-Berkeley. The spectral resolution across most of the 905–1220 Å bandpass is roughly 100 $\mathrm{km\,s^{-1}}$ (FWHM). We resampled the data into 0.1 Å bins to produce a spectrum with S/N ≈ 7 per resolution element near 1030 Å. The absolute wavelength uncertainty of the data processing is roughly 0.5 Å, but we were able to improve upon this to an accuracy of ≈ 0.1 Å (30 $\mathrm{km\,s^{-1}}$ at 1000 Å) by noting the positions of lines in the H_2 Lyman series (0–0) to (8–0) vibrational bands across the spectrum.

The fully reduced ORFEUS-II spectrum is shown in Figure 2. The far-ultraviolet continuum of ESO 141-055 is relatively flat, with a rise centered near $\sim$1075 Å corresponding to the broad-line O VI emission from the AGN. We have identified the locations of some of the interstellar atomic lines of interest in the figure. Most of the remaining unlabeled features are lines of H_2. The main diagnostic of hot gas visible in the spectrum is the O VI doublet, with lines at 1031.93 and 1037.62 Å. Inspection of the O I λ1039.23 line near the weaker member of the O VI doublet confirms that the zero-point of the wavelength scale in the O VI spectral region is consistent with that derived from the H_2 lines.

For information about the design and far-ultraviolet performance of the Berkeley spectrograph, see Hurwitz & Bowyer (1996) and Hurwitz et al. (1998b). Descriptions of the Astro-SPAS platform and ORFEUS project have been given by Grewing et al. (1991).

3. Absorption Line Measurements

We fit continua to the spectra shown in Figures 1 and 2 using Legendre polynomials defined over wavelength regions free from obvious interstellar absorption lines. Equivalent

widths and errors for the high ion lines and the Si II and S II lines present in the GHRS spectra are listed in Table 1. We also list the central velocities and full widths at half maximum intensity for each line. Discussions of continuum placement and equivalent width determination methods can be found in Sembach & Savage (1992). The normalized line profiles are shown in Figure 3.

3.1. The Ultraviolet Lines Between 1230 Å and 1555 Å

The GHRS data are of sufficient quality to permit ion-ion profile comparisons as a function of velocity. This is most readily done by converting the observed absorption profiles into apparent column density profiles in units of ions cm^{-2} $(\mathrm{km\,s}^{-1})^{-1}$ through the relation

$$N_a(v) = \frac{m_e c}{\pi e^2}\,\frac{\tau_a(v)}{f\lambda} = 3.768 \times 10^{14}\,\frac{\tau_a(v)}{f\lambda}, \tag{1}$$

where

$$\tau_a(v) = ln\frac{I_c(v)}{I_{obs}(v)} \tag{2}$$

is the apparent optical depth of the line as a function of velocity v. In Eqs.(1) and (2) $I_c(v)$ and $I_{obs}(v)$ are the estimated continuum and observed intensities at v, f is the oscillator strength of the line, and λ is the wavelength of the line in Å. We can check for unresolved saturated structure at different velocities by comparing the profiles of multiple lines of the same species differing in the product $f\lambda$ (see Savage & Sembach 1991). We show the $N_a(v)$ profiles for the S II, Si IV, C IV, and N V lines in Figure 4, where it can be seen that there is general agreement between the $N_a(v)$ profiles of the weaker line (solid line) and the stronger line (filled circles) of each species over most of the velocity range shown. However, at some velocities, particularly those near the column density peaks, the $N_a(v)$ profiles of the stronger lines underestimate the $N_a(v)$ profiles of the weaker lines, thereby indicating that unresolved saturated structure exists at those velocities.

We list the integrated apparent column densities of the ions in column 8 of Table 1. These integrations were defined by $N_a = \int N_a(v)\,\mathrm{dv}$ over the velocity ranges listed in column 4. Comparison of the integrated values of N_a for individual lines of a given species also indicates that modest saturation corrections are needed for C IV and Si IV. Application of saturation corrections based upon the N_a values for each species results in the final

column densities listed in column 9. These values were derived using the integrated values of N_a (see Savage & Sembach 1991) and are consistent with the pixel-by-pixel saturation correction algorithm described by Jenkins (1996).[4]

In the case of the broad, weak lines of N V, we have simply averaged the values of N_a to produce a final value of $N(\mathrm{N\ V}) \approx 6.65 \times 10^{13}$ cm^{-2}. It is unlikely that there are narrow components with $\tau \gg 1$ in these profiles. The ionization potential for the creation of N V is 77.5 eV, and most of the N V is probably collisionally ionized in hot (T $\gtrsim 10^5$ K) gas.

We note the presence of weak Mg II $\lambda\lambda$1239.925, 1240.395 absorption near N V. These lines are indicated in Figures 1 and 3. There may also be a small amount ($W_\lambda < 150$ mÅ) of CO $(\mathrm{A–X})_{0-0}$ band absorption near 1544.5 Å. Combined with $W_\lambda < 70$ mÅ for the $(\mathrm{A\text{-}X})_{5-0}$ band near 1392.5 Å, we set a 2σ limit of log $N(\mathrm{CO}) \lesssim 4 \times 10^{14}$ cm^{-2}. The only other noticeable absorption feature in the GHRS spectra is a redshifted Lyα line at 1258.126 Å ($z = 0.03492$). This line has $W_\lambda(\mathrm{Ly}\alpha) \approx 220$ mÅ, which places it on the flat part of the curve-of growth. The absorber is probably associated with ESO 141-055 given the similarity in the redshifts of the two objects.

3.2. The Far Ultraviolet Lines

The far-ultraviolet spectrum of ESO 141-055 shown in Figure 2 reveals a rich set of absorption lines due to both atomic and molecular species. At the spectral resolution of the ORFEUS-II data (≈ 100 km s^{-1}), many of the features, including the O VI lines, are blended with nearby lines. To determine the possible effects of this blending on the amount of O VI derived for the sight line, we have replotted the 1000–1100 Å ORFEUS-II data in Figure 5. Atomic lines near the O VI lines include C II λ1036.34, C II* λ1037.02, and multiple lines in the (6–0) and (5–0) vibrational bands of H_2 between 1031.5–1032.5 Å and 1036.5–1038.7 Å (Morton 1991; Sembach 1999).

We created a simple model of the neutral gas absorption along the sight line. Using the GHRS Si II and S II line profiles as a template for the neutral atomic gas velocity distribution, we simulated the absorption with the following parameters: $N(\mathrm{H\ I}) = 3.5 \times 10^{20}$ cm^{-2}, b = 28 km s^{-1}, and $v_{\mathrm{LSR}} = 0$ km s^{-1}. The model does not include ionized gas. The total H I column density of 3.5×10^{20} cm^{-2} provides reasonable agreement with the observed

[4]The S/N of our data is too low to trust saturation corrections derived from the Jenkins (1996) method for individual pixels, but an integration of the corrected profiles yields a result similar to the one obtained by applying the Savage & Sembach (1991) correction. This is expected since the saturation corrections are modest.

Lyβ absorption, the amount of H I expected for a low latitude extragalactic sight line (Savage et al. 1997), the approximate S/H ratio for a halo sight line [N(S II)/N(H I) $\approx$ (0.5–1.0) $\times$(N(S)/N(H))$_\odot$] (Savage & Sembach 1996)[5], and the H I column of $\sim$5$\times$10^{20} cm^{-2} derived from the H I 21 cm emission data of Colomb, Poppel, & Heiles (1980)[6]. The model is represented by the heavy solid line overplotted on the spectrum in Figure 5. At the resolution of the data, the precise details of the model velocity distribution do not strongly affect our primary conclusions. The absorption lines in the model were constructed using solar reference abundances (Anders & Grevesse 1989; Grevesse & Noels 1993) and atomic data compiled by Morton (1991).

We have also included a molecular component in the model shown in Figure 5 to reproduce the numerous H_2 lines observed. A single component with $N(H_2) = 1\times10^{19}$ cm^{-2}, b = 10 km s^{-1}, $v_{\rm LSR} = 0$ km s^{-1}, and T$_{rot}$ = 100 K reproduces many of the observed absorption features well. The column density and rotational temperature of the molecular component can be varied by roughly $\pm^{2.0}_{0.5}\times10^{19}$ cm^{-2} and $\pm$20° K, respectively, before the fits become noticeably discrepant from the data. Lower temperature models underproduce the amount of H_2 in the J $\geq$ 2 levels, while higher temperature models overproduce higher J level absorption. In the adopted model, 38% of the H_2 is in the J = 0 level, 61% is in the J = 1 level, and 1% is in the J = 2 level. Adopting a lower b-value for the molecular gas requires a higher value of $N(H_2)$ to match the data. Higher resolution data are needed to determine the velocity distribution of the molecular gas and reliable column densities in each rotational level.

It is clear from the model shown in Figure 5 that atomic lines of Si II, Ar I, and Fe II should be strong unless the elements are depleted from the gas onto dust or are ionized into higher ionization stages. Of special note is the apparent absence of strong absorption by Fe II and Ar I. Lines of these species are indicated with asterisks below the spectrum in Figure 5. We discuss these lines further in §5.

Of the two members of the O VI doublet, the 1031.93 Å line is less susceptible to blending with other lines and is strong in this spectrum. Note the possible presence of the 1031.19 Å (6–0) P(3) line of H_2 in the blue wing of the O VI line at a velocity of –214 km s^{-1}. Integrating over the –150 to +100 km s^{-1} velocity range, we find W$_\lambda$(1031.93) $\approx$ 537$\pm$100

[5]The column density of S I along the sight line is small, log N(S I) < 14.09 (Table 1). Thus, N(S I)/N(S II) < 0.04.

[6]The half-power beam width for the 21 cm radio observations is 30′. Therefore, there may be additional H I emission contributing to the 21 cm profile from regions near to, but not directly along, the sight line sampled by the absorption measurements (see §6).

mÅ, which converts to a logarithmic column density $\log N(\mathrm{O\ VI}) = 15.1 \pm^{0.6}_{0.3}$, assuming the absorption can be described by a single component with a width $\mathrm{b} \approx 57 \pm 8$ km s^{-1} derived by fitting a single Gaussian component to the N V lines. A velocity component distribution having several narrower components resembling those seen in the C IV profiles produces a similar result. O VI λ1037.62 is severely blended with strong C II absorption centered near –370 km s^{-1} and the R(0), R(1), and P(1) lines of the (5–0) Lyman series vibrational band of H_2 centered at –311, –135, and +157 km s^{-1}, respectively. We do not consider the O VI 1037.62 Å line further in this study.

We find only marginal evidence for Lyβ absorption at 1061.54 Å associated with the $z = 0.03492$ Lyα absorber seen in our GHRS spectrum. For this absorber, we estimate that $\mathrm{W}_\lambda(\mathrm{Ly}\beta) \approx 120 \pm 70$ mÅ, which together with the Lyα measurement (§3.1) suggests a total column density of $\log N(\mathrm{H\ I}) = 13$–16. The unidentified absorption feature near 1041.2 Å is unlikely to be a Lyβ line from an intergalactic cloud at redshift $z = 0.0151$ since there is no corresponding Lyα absorption at 1234.0 Å in Figure 1 ($\mathrm{W}_\lambda < 40$ mÅ, $N(\mathrm{H\ I}) < 7.3 \times 10^{12}$ cm^{-2}).

4. High Ionization Gas

4.1. Scale Heights

The integrated column densities of the high ionization species observed toward ESO 141-055 are consistent with an extended distribution of highly ionized gas away from the Galactic plane. Assuming an exponential density distribution given by $\mathrm{n(z)} = \mathrm{n_0\, e^{-|z|/h_z}}$, the integrated column density of an ion in a direction perpendicular to the Galactic disk is $N_\perp(\mathrm{ion}) = N(\mathrm{ion}) \sin|b| = \mathrm{n_0} h_z$. Values of $N_\perp$ for the highly ionized species toward ESO 141-055 are listed in Table 2 along with values for the sight lines to HD 36402 (in the LMC), PKS 2155-304, and 3C 273. Table 2 also contains the results of fitting exponential distributions to the values of $N_\perp$ for Si IV, C IV, and N V for an ensemble of sight lines toward ∼10 AGN/QSOs and ∼30 OB stars (Savage et al. 1997). The ESO 141-055 values are systematically higher than the Galactic averages by ∼0.1–0.3 dex, but are less than those toward 3C 273, which may have a substantial high ion contribution arising within Galactic Radio Loops I and IV (see Sembach et al. 1997).

Values of $N_\perp$(O VI) have been measured for only a few sight lines through the Galactic halo. The directions studied include 4 LMC and 2 SMC sight lines (Hurwitz et al. 1995; Widmann et al. 1998), PKS 2155-304 (Hurwitz et al. 1995), and 3C 273 (Davidsen 1993; Hurwitz et al. 1998a). This has made it difficult to determine an O VI scale height that

can be generalized to the Galaxy as a whole. Indeed, values of h_z ranging from a low of $\sim$100 parsecs (Jenkins 1978a,b; Hurwitz & Bowyer 1996) up to $\sim$5 kiloparsecs (Widmann et al. 1998) have been reported in the literature. As more data become available both for extended sight lines in the Galactic disk and sight lines through the Galactic halo, it will be possible to place better constraints on n_0 and h_z. The results for ESO 141-055 favor a scale height on the order of the scale heights found by Savage et al. (1997) for the other high ions: h_z(Si IV) $\approx$ 5.1 kpc, h_z(C IV) $\approx$ 4.4 kpc, and h_z(N V) $\approx$ 3.9 kpc. Assuming n_0(O VI) ≈ 1–2×10^{-8} ions cm^{-2} from local estimates of N(O VI) made with the Copernicus satellite (Shelton & Cox 1994), the ESO 141-055 value of $N_\perp$(O VI) $\approx 4.5\times10^{14}$ cm^{-2} implies h_z(O VI) $\approx$ 7–14 kpc. If n_0(O VI) is as high as 5×10^{-8} ions cm^{-2} (Hurwitz & Bowyer 1996), then the inferred value of h_z(O VI) becomes $\approx$3 kpc.

Patchiness in the gas distribution complicates scale height determinations and necessitates determinations of $N_\perp$ for an ensemble of sight lines before meaningful estimates of h_z and its error can be made and applied to more general problems. Several lines of evidence point to a clumpy distribution for the O VI-bearing gas in the Galactic disk and halo. The values of $N_\perp$(O VI) in Table 2 indicate that there is at least a factor of $\sim$4 range in the O VI columns perpendicular to the disk in the inner regions of the Galaxy. This spread is comparable to the patchiness found for C IV and N V at many distances from the Galactic plane over large angular scales (Savage et al. 1997). Over small angular separations, the limited data suggest that $N_\perp$(O VI) may vary more than $N_\perp$(C IV). For example, $\Delta N_\perp$(O VI) is at least a factor of 3.7 between LMC and SMC directions, compared to $\Delta N_\perp$(C IV) $\approx$ 2.0. Additional evidence for patchiness of the O VI distribution comes from a study of ORFEUS-I spectra for halo stars by Hurwitz & Bowyer (1996), who found low columns of O VI out to $|z| < 3$ kpc.

ESO 141-055 intercepts Radio Loop I near its southern boundary (Berkhuijsen, Haslam, & Salter 1971). The large amount of high ion gas observed may be due in part to passage of the sight line through this structure (see Sembach et al. 1997), but some of the O VI absorption could be associated with more distant regions. The sight line also passes through the 3/4 keV X-ray enhancement attributed to the Galactic bulge (Snowden et al. 1995). Observations of O VI along other sight lines in this region of the sky will be needed to separate foreground absorption produced by Loop I from the contributions of more distant regions.

4.2. Velocity Structure

The high ionization lines of Si IV and C IV (and to a lesser degree N V) have a velocity structure indicative of multiple components over the LSR velocity range from –130 to +140 km s^{-1}. Distinct features can be seen at $v_{\rm LSR} \approx$ –60, +15, and +45 km s^{-1} (Figure 3). The profiles also show a positive velocity wing extending to $\approx$+120 km s^{-1}. In this direction, differential Galactic rotation can result in negative line-of-sight velocities out to a distance of 17 kpc (z = –8 kpc). We show the rotation curve for a co-rotating gas distribution along the sight line in the top right panel of Figure 6. The minimum predicted velocity of –103 km s^{-1} occurs at d = 8.8 kpc (z = –4.0 kpc, R_g = 3.1 kpc).[7]

The ESO 141-055 sight line passes through the inner regions of the Galaxy at a minimum galactocentric radius of 3.1 kpc, where non-circular motions may confuse the absorption signature expected for gas participating in differential Galactic rotation. Previous studies of the high ion absorption toward inner Galaxy stars in this general direction (Savage, Massa, & Sembach 1990; Sembach, Savage, & Massa 1991; Sembach, Savage, & Lu 1995; Savage, Sembach, & Cardelli 1994) have shown that the highly ionized ISM is complex, with kinematics varying as a function of distance from the Galactic plane. Possible explanations for the presence of "forbidden velocity" gas in the inner Galaxy have been summarized by Tripp, Sembach, & Savage (1993).

To determine the nature of the gas distribution along the ESO 141-055 sight line, we have constructed several simple models for a smoothly distributed gas having an exponentially declining density with distance from the Galactic plane. We have created the apparent column density profiles expected for several values of the intrinsic gas velocity dispersion (σ = 10, 20, 30 km s^{-1}) and gas scale height (h_z = 1, 5, 10 kpc). These profiles are shown in Figure 6 along with the C IV $N_a(v)$ profiles for the ESO 141-055 sight line and for four sight lines toward stars in the inner Galaxy. The locations of the sight lines are shown schematically in Figure 7. Several conclusions can be drawn from a direct comparison of the ESO 141-055 profile to the other profiles.

(1) None of the stellar sight lines shows the strong peak in C IV near +15 km s^{-1} seen toward ESO 141-055. This feature cannot be reproduced in the smooth gas model profiles without causing serious disagreement at other velocities. The high ion gas at these velocities might be associated with the low ion (and perhaps molecular) gas near +5 km s^{-1}. As expected, the ESO 141-055 sight line exhibits less total C IV absorption than the extended, lower latitude sight lines shown in Figure 6.

[7] R_g is the distance from the Galactic center of the projection of the sight line onto the Galactic plane.

(2) The ESO 141-055 sight line has a C IV extension to negative velocities comparable to that of the HD 151990, HD 156359, and HD 163522 sight lines. However, the positive velocity wing is seen only toward the two stars located at smaller Galactic longitudes (HD 151990 and HD 156359). The smooth gas distribution models shown in the right panel of Figure 6 indicate that substantial column densities at positive velocities are expected for corotating gas only if the scale height is large ($h_z > 5$ kpc). The presence of the positive velocity wing toward HD 151990, which attains a maximum z-distance of 430 pc, suggests that the positive velocity absorption toward ESO 141-055 may actually occur within a few hundred parsecs of the disk. Alternatively, if deviations from corotation are present in the low halo as suggested by Sembach et al. (1991) for the HD 156359 sight line, the absorption may occur at higher altitudes (z = 1–2 kpc).

(3) The smooth gas distribution models shown in Figure 6 can roughly reproduce the observed C IV $N_a(v)$ profile toward ESO 141-055 if the strong absorption near +15 km s^{-1} is attributed to an additional enhancement along the sight line. The best fit parameters ignoring the +15 km s^{-1} feature are n_0(C IV) = 4.0×10^{-9} cm^{-2}, h_z(C IV) = 11.5 kpc, and σ(C IV) = 30 km s^{-1}. Similar values of h_z and σ are obtained when the N V $N_a(v)$ profiles are modeled. The major shortcoming of this model is the overprediction in the amount of C IV and N V at $v_{\rm LSR} < -80$ km s^{-1}. While the high ion scale height derived from this kinematical analysis is roughly consistent with the large value inferred from the $N \sin |b|$ considerations for O VI (§4.1), such a large scale height is out of character when other sight lines through the Galactic center are considered (see Savage et al. 1997). We conclude that there is either an enhancement in the high ion columns along the ESO 141-055 sight line compared to these other inner Galaxy sight lines, or that the global distribution of gas in the region of the Galactic center is irregular. In either case, the highly ionized gas distribution is patchy in nature, so it is unwise to draw Galaxy-wide conclusions from the analysis of observations of a small number of lines of sight.

4.3. Ionization

Of the ions observed in this study, O VI is the best tracer of gas at coronal temperatures. It peaks in abundance in collisional ionization equilibrium at ∼2.8×10^5 K, compared to 1.8×10^5 K, 1.0×10^5 K, and 6.3×10^4 K for N V, C IV, and Si IV, respectively (Sutherland & Dopita 1993). Furthermore, the predicted strengths of the O VI lines are often several times those of the C IV and N V lines. O VI traces gas at temperatures up to ∼10^6 K and is not produced in significant quantities by photoionization in the ambient ISM (Benjamin & Shapiro 1999).

The velocity resolution of our ORFEUS-II data does not allow us to determine the O VI column densities of individual absorbing regions along the ESO 141-055 sight line. However, it is possible to compare the integrated strength of the O VI absorption to the other high ions and derive information about the sight-line-averaged ionization conditions in this direction. The high ion ratios are listed in Table 3, where they are compared to values for other sight lines and to theoretical predictions. The high ion ratios toward ESO 141-055 are marginally higher than those observed toward 3C 273.

The N(C IV)/N(O VI) ratio is suggestive of a mix of disk and halo gases along the ESO 141-055 sight line. The observed value of 0.55±0.30 is near the high end of values found for the Galactic disk and the low end of values for the Galactic halo (Spitzer 1996). A similar conclusion is reached if N V and O VI are compared. We find N(O VI)/N(N V) ≈ 15, which is the same as the average value found for the Galactic disk by Hurwitz & Bowyer (1996).

The radiatively cooling fountain flow model proposed by Benjamin & Shapiro (1999) to explain the presence of highly ionized gas in the Galactic halo provides a reasonable description of the integrated high ion ratios toward ESO 141-055 (see Table 3). A combination of turbulent mixing layers (Slavin, Shull, & Begeleman 1993) and conductive interfaces (Borkowski, Balbus, & Fristrom 1990) in the right proportions could also reproduce the observed values. Evidence for an interaction of hot and cool (or warm) gases is provided by the apparent column density profiles shown in Figure 4. The high ion profiles have a noticeable peak near $v_{\rm LSR} \approx +15$ km s^{-1}, which is near the peak of the S II profiles. The observed ratio N_a(C IV)/N_a(Si IV) $\approx$ 4–5 is roughly constant over the –100 to +100 km s^{-1} velocity range, but is likely to be somewhat higher near –60 km s^{-1} and +15 km s^{-1} due to modest saturation corrections required for C IV at those velocities. Hybrid descriptions of the hot gas distribution in the Milky Way have been suggested to explain the high ion observations (e.g., Shull & Slavin 1994; Spitzer 1996), but it is difficult to distinguish among the many possible combinations without a significantly larger data set for O VI than now exists. We anticipate that FUSE will fill this vital need and shed new light on the issue of the ionization of the disk and halo gases.

5. Low Ionization Gas

The amount of high-resolution information for the low ionization interstellar gas toward ESO 141-55 is limited. The Mg II λ1240 doublet lines are weak – $W_\lambda \approx 50$ mÅ, log N(Mg II) $\sim 5 \times 10^{15}$ cm^{-2}. The absorption lines of Si II and S II attain maximum depth near $\sim$+5 km s^{-1}. The S II lines have a weak, negative velocity wing that could

be associated with some of the higher ionization gas (see Figure 3). The overall velocity extents of the Si II λ1260.42 line and the high ion lines are similar. However, unlike the high ion profiles, which are stronger at –50 km s^{-1} than at +50 km s^{-1}, Si II $\lambda\lambda$1260.42, 1526.71 exhibit much stronger absorption at positive velocities than the high ions. Note that Si II λ1260.42 includes blended Fe II λ1260.53 absorption centered near +26 km s^{-1}.

Several conclusions can also be drawn from a comparison of the ORFEUS-II data and the model fit shown in Figure 5. First, atomic lines of H I (Lyβ), C II, O I, Si II, Ar I, and Fe II should be present unless the elements are depleted from the gas onto dust or ionized into higher ionization stages. H I, C II, O I, and Si II are all clearly detected. We find W$_\lambda$(Si II λ1020.7) $\approx$ 380$\pm$140 mÅ and W$_\lambda$(O I λ1039.2) $\approx$ 470$\pm$105 mÅ. Absorption by Fe II or Ar I is not as strong as predicted by the model. Fe is easily incorporated into grains, and even in the warm neutral ISM of the Galactic halo is depleted by a factor of $\sim$5 (see Savage & Sembach 1996). Depletion factors of refractory elements in the warm ionized ISM appear to be comparable (Howk & Savage 1999). Thus, the absence of gas-phase Fe II could be explained by the presence of dust. However, the absence of Ar I absorption cannot be so readily explained by depletion effects since Ar is a noble element, and its abundance is probably not affected significantly by depletion (see Jenkins 1987). Sofia & Jenkins (1998) considered the ionization of Ar by starlight and found that Ar I is highly susceptible to photoionization in low-density, partially ionized regions. For a dilute gas that is approximately half ionized, they estimated that N(Ar I)/N(H I) can be as small as 0.1 times the solar value of N(Ar)/N(H).

If we assume that all of the Ar I and S II along the sight line arises in H I regions and N(Ar I)/N(S II) $\approx$ (N(Ar)/N(S))$_\odot$ = 0.195, then we expect log N(Ar I) $\approx$ 14.74. For single absorption components with b-values of 5, 10, and 30 km s^{-1}, this column density corresponds to equivalent widths of 72, 131, and 323 mÅ for the Ar I 1048.2 Å line. (The model line shown in Figure 5 has W$_\lambda$ = 363 mÅ.) Integrating over the $\pm$200 km s^{-1} velocity range, we find W$_\lambda$(Ar II λ1048.2) $<$ 200 mÅ. There could be a substantial amount of Ar I hiding in the ORFEUS-II spectrum provided that the b-value of the Ar I is lower than about 20 km s^{-1}. Partial photoionization of the gas would reduce the expected amount of Ar I relative to S II since Ar I traces mainly H I gas, whereas S II traces both H I and H II region gas.

Trying to resolve this ionization issue would be valuable since the nature of ionizing sources in the Galactic halo is still poorly understood. The sight line is confined to the Galactic disk ($|z| < 500$ pc) for only $\sim$1 kpc. Hα measurements reveal that the diffuse ionized gas in the Galaxy, which has a scale height of $\sim$1 kpc and a filling factor of roughly 20%, is probably photoionized by photons from O stars (Reynolds 1993). Ions in the

900–1200 Å wavelength range that could be used to study the ionization conditions include N I-II, P II-V, Ar I-II, and Fe II-III. The S/N and spectral resolution of our ORFEUS-II data do not allow these types of comparisons.

6. Molecular Gas

It is generally believed that extended sight lines through the Galactic halo are low density paths containing little cold atomic or molecular gas. It is therefore interesting that the far-ultraviolet spectrum of ESO 141-055 shown in Figures 2 and 5 shows clear evidence of absorption due to H_2. The average H I density is roughly 0.11 atoms cm^{-2}, assuming $N(\mathrm{H\ I}) = 3.5{\times}10^{20}$ atoms cm^{-2} and a 1 kpc path length. The H_2 column density is roughly $1{\times}10^{19}$ molecules cm^{-2}, which corresponds to a sight-line-averaged molecular gas fraction $f_{H_2} = 2N(H_2) \,/\, [2N(H_2){+}N(\mathrm{H\ I})] \approx 0.05$. This value of f_{H_2} is typical of the sight lines with color excesses E(B-V) $\approx$ 0.1 mag surveyed by Savage et al. (1977). Most of the molecular gas likely arises within a single component since a column density of $N(\mathrm{H}) \sim 5{\times}10^{20}$ cm^{-2} is needed to effectively self-shield the H_2 from the interstellar UV radiation field (Savage et al. 1977). The H_2 absorption probably occurs at a velocity near the peak of the S II absorption shown in Figure 4. The marginal detection of CO near 1544.5 Å (Figure 1, §3.1) is qualitatively consistent with such a velocity.

A possible site for the H_2 absorption is shown in Figure 8. The sight line lies within an enhancement in the dust distribution revealed by 100μm emission in the IRAS Sky Survey Atlas (Wheelock et al. 1994). The 100μm feature is approximately 1° across and appears loosely connected to similar features in this region of the sky. The intensity of the 100μm emission along the sight line is 5.0 MJy sr^{-1}, which exceeds the intensity of 88% of the pixels in the 7.5°×7.5° field shown. Note that the intensity of the emission changes rapidly over angular scales of 10–15 arc minutes. Using the approximate relation $<I_{100}/N(\mathrm{H})> \approx (1.0 \pm 0.3) \times 10^{-20}$ MJy sr^{-1} cm^2 appropriate for the infrared cirrus (Reach, Koo, & Heiles 1994), we find that the 100μm emission in this feature corresponds to $N(\mathrm{H}) \approx (3.5 - 6.5) \times 10^{20}$ cm^{-2}. This feature is probably an important source of H I as well as H_2 along the sight line. The distance of the cloud is unknown, but typically molecular clouds are within ∼300 pc of the disk (Dame & Thaddeus 1994), which translates to a distance of <700 pc in this direction.

The H_2 gas along the ESO 141-055 sight line can be modeled as a relatively cold ($T_{rot} \approx 100$ K) cloud (see §3.2). Non-equilibrium population of the rotational levels may also be important, especially if strong sources of UV radiation exist in the halo. ORFEUS-I observations of H_2 toward several early type stars located at distances of 1–4 kpc within

the Galactic disk revealed H_2 column densities about a factor of 10 higher than the H_2 column density along the ESO 141-055 sight line. Those clouds have similar temperatures ($T_{rot} \approx 80$–100 K) and molecular hydrogen fractions ($f_{H_2} \approx 0.06$–0.16) (Dixon, Hurwitz, & Bowyer 1998). Thus, the overall amount and general properties of the H_2 toward ESO 141-055 are consistent with what is expected for an extended, moderate latitude sight line. In this context, we note that ORFEUS-II observations of the 3C 273 sight line, which is located at $b = +64.4°$, revealed at modest statistical significance a much lower column of H_2 ($\sim 10^{15}$ cm^{-2}) (Hurwitz et al. 1998a). Further determinations of the properties of the molecular gas toward ESO 141-055 and along other halo sight lines would provide an important benchmark for studies of H_2 in the Magellanic Clouds (Richter et al. 1998, de Boer et al. 1998) and quasar absorption line systems (Foltz, Chaffee, & Black 1988; Ge & Bechtold 1997).

7. Conclusions

We present GHRS and ORFEUS-II absorption line data of the high ionization lines of Si IV, C IV, N V, and O VI in the ISM of the Galactic disk and halo toward ESO 141-055 ($l = 338.18°$, $b = -26.71°$). We find that the high ionization absorption is strong, with integrated high ion column density ratios consistent with the signature expected for radiatively cooling gas in a "Galactic fountain" or an inhomogeneous ISM containing conductive interfaces and turbulent mixing layers. The O VI column density perpendicular to the Galactic plane, $N\sin|b| \approx 4.5 \times 10^{14}$ cm^{-2}, suggests that the scale height of O VI is large ($\gtrsim$3 kpc), but further work is needed to generalize this result to other regions of the Galaxy. Models of the velocity distribution of the C IV absorption toward ESO 141-055 are also consistent with a large high ion scale height, though they cannot reproduce all of the structure observed in the C IV profiles. Some of the high ion absorption along the sight line may occur in the Galactic bulge region, which emits strongly at soft X-ray wavelengths. Comparison of the ESO 141-055 high ion column densities with those of other sight lines indicates that the O VI distribution is at least as patchy as that of C IV.

Low ionization absorption lines are also detected toward ESO 141-055. The strengths of these lines in the ORFEUS-II spectrum are difficult to gauge with the available data, but it appears that Ar I is considerably weaker than expected. The sight line intercepts a cold molecular cloud containing $\approx 10^{19}$ molecules cm^{-2} of H_2, which produces easily identifiable (and somewhat confounding) blends of absorption at the 100 km s^{-1} resolution of the ORFEUS-II data. High-resolution FUSE observations of this sight line would be of considerable value in sorting out the velocity structure and physical conditions in the

molecular, cold atomic, and highly ionized ISM along the sight line.

We thank Steve Federman for useful comments on the manuscript. We acknowledge use of the SkyView data browser available on the internet at the Goddard Space Flight Center (http://skyview.gsfc.nasa.gov/skyview.html). KRS acknowledges support from NASA Long Term Space Astrophysics grant NAG5-3485 and from the FUSE project through grant NAS5-32985. BDS appreciates support from NASA through grant GO-06451.01-95A from the Space Telescope Science Institute. MH acknowledges support from NASA grant NAG5-696.

REFERENCES

Anders, E. & Grevesse, N. 1989, Geochim. Cosmochim. Acta, 53, 197

Benjamin, R. & Shapiro, P. 1999, ApJS, submitted

Berkhuijsen, E., Haslam, C.G.T., & Salter, C.J. 1971, A&A, 14, 252

Borkowski, K.J., Balbus, S.A., & Fristrom, C.C. 1990, ApJ, 355, 501

Brandt, J.C., et al. 1994, PASP, 106, 890

Burles, S. & Tytler, D. 1996, ApJ, 460, 584

Cen, R. & Ostriker, J.P. 1999, ApJ, 514, 1

Cleary, M.N., Heiles, C., & Haslam, C.G.T. 1979, A&AS, 36, 95

Clemens, D.P. 1985, ApJ, 295, 422

Colomb, F.R., Poppel, W.G.L., & Heiles, C. 1980, A&AS, 40, 47

Dame, T.M. & Thaddeus, P. 1994, ApJ, 436, L173

Davidsen, A.F. 1993, Science, 259, 327

de Boer, K.S., Richter, P., Bomans, D.J., Heithausen, A., & Koorneef, J. 1998, A&A, L5

de Vaucouleurs, G., de Vaucouleurs, A., Corwin, H.G. Jr., Buta, R.J., Pautrel, G., & Fougue, P. 1991, Third Reference Catalogue of Bright Galaxies, v3.9

Dixon, W.V., Hurwitz, M., & Bowyer, S. 1998, ApJ, 492, 569

Dufton, P.L., Hibbert, A., Kingston, A.E., & Tully, J.A. 1983, MNRAS, 202, 145-50

Federman, S.F. & Cardelli, J.A. 1995, ApJ, 452, 269

Foltz, C.B., Chaffee, F.H., & Black, J.H. 1988, ApJ, 324, 267

Ge, J & Bechtold, J. 1997, ApJ, 477, L73

Grevesse, N. & Noels, A. 1993, in Origin of the Elements, eds. N. Prantzos, E. Vangioni-Flam, & M. Cassé (Cambridge: Cambridge University Press), 15

Grewing, M., et al. 1991, in Extreme Ultraviolet Astronomy, eds. R.F. Malina & S. Bowyer (Elmsford: Pergamon), 437

Heap, S.R., et al. 1995, PASP, 107, 871

Howk, J.C. & Savage, B.D. 1999, ApJ, in press

Hurwitz, M. & Bowyer, S. 1996, ApJ, 465, 296

Hurwitz, M., Bowyer, S., Kudritski, R.P., & Lennon, D.J. 1995, ApJ, 450, 149

Hurwitz, M., Appenzeller, I., Barnstedt, J., Bowyer, S., Dixon, W.V., et al. 1998a, ApJ, 500, L61

Hurwitz, M., Bowyer, S., Bristol, W., Dixon, W.V., Dupuis, J., et al. 1998b, ApJ, 500, L1

Jenkins, E.B. 1978a, ApJ, 219, 845

Jenkins, E.B. 1978b, ApJ, 220, 107

Jenkins, E.B. 1987, in Interstellar Processes, eds. D.J. Hollenbach & H.A. Thronson, Jr. (Dordrecht: Reidel), 533

Jenkins, E.B. 1996, ApJ, 471, 292

Lu, L., Savage, B.D., Tripp, T.M., & Meyer, D.M. 1995, ApJ, 447, 597

Mihalas,D. & Binney, J., 1981, Galactic Astronomy, 2^{nd} edition (San Francisco: Freeman)

Morton, D.C. 1991, ApJS, 77, 119

Reach, W.T., Koo, B-C., & Helies, C. 1994, ApJ, 429, 672

Reynolds, R.J. 1993, in Back to the Galaxy, ed. S. Holt & F. Verter (New York: American Institute of Physics), 156

Richter, P., Widmann, H., de Boer, K.S., Appenzeller, I., Gölz, M., et al. 1998, A&A, L9

Robinson R.D., et al. 1998, PASP, 110, 68

Savage, B.D., Bohlin, R.C., Drake, F.J., & Budich, W. 1977, ApJ, 216, 291

Savage, B.D., Massa, D, & Sembach, K.R. 1990, ApJ, 355, 14

Savage, B.D. & Sembach, K.R. 1991, ApJ, 379, 245

Savage, B.D. & Sembach, K.R. 1996, ARA&A, 34, 279

Savage, B.D., Sembach, K.R., & Cardelli, J.C. 1994, ApJ, 420, 183

Savage, B.D., Sembach, K.R., & Lu, L. 1997, AJ, 113, 2158

Savage, B.D., Tripp, T.M., & Lu, L. 1998, AJ, 115, 436

Schectman, R.M., Povolny, H.S., & Curtis, L.J. 1998, ApJ, 504, 921

Sembach, K.R. 1999, in the Proceedings of the Stromlo Workshop on High Velocity Clouds, eds. B.K. Gibson & M.E. Putnam, ASP Conf. Series (San Francisco: ASP), 243

Sembach, K.R. & Savage, B.D. 1992, ApJS, 83, 147

Sembach, K.R., Savage, B.D, & Lu, L. 1995, ApJ, 439, 672

Sembach, K.R., Savage, B.D., & Massa, D. 1991, ApJ, 372, 81

Sembach, K.R., Savage, B.D., & Tripp, T.M. 1997, ApJ, 480, 216

Shelton, R.L. & Cox, D.P. 1994, ApJ, 434, 599

Shull, J.M. & Slavin, J.D. 1994, ApJ, 427, 784

Slavin, J.D., Shull, J.M., & Begelman, M.C. 1993, ApJ, 407, 83

Snowden, S.L., Freyberg, M.J., Plucinsky, P.P., Schmitt, J.H.M.M., Truemper, J., et al. 1995, ApJ, 454, 643

Soderblom, D.R., Hulbert, S.J., Leitherer, C., & Sherbert, L.E. 1994, Goddard High Resolution Spectrograph Instrument Handbook, v5 (Baltimore: Space Telescope Science Institute)

Sofia, U.J. & Jenkins, E.B. 1998, ApJ, 499, 951

Songaila, A. & Cowie, L.L. 1996, AJ, 112, 335

Spitzer, L. 1990, ARA&A, 28, 71

Spitzer, L. 1996, ApJ, 458, L29

Steidel, C.C. 1990, ApJS, 72, 1

Sutherland, R.S. & Dopita, M.A. 1993, ApJS, 88, 253

Tripp, T.M., Sembach, K.R., & Savage, B.D. 1993, ApJ, 415, 652

Wheelock, S.L., et al. 1994, IRAS Sky Survey Atlas: Explanatory Supplement (Pasadena: Jet Propulsion Laboratory)

Widmann, H., de Boer, K.S., Richter, P., Krämer, G., Appenzeller, I., et al. 1998, A&A, 338, L1

Figure Captions

Fig. 1. – GHRS G160M spectra of the N V, Si IV, and C IV spectral regions of ESO 141-055. The data have S/N ≈ 13–21 per resolution element and spectral resolutions (FWHM) of 14–18 $\mathrm{km\,s^{-1}}$. Error spectra (1σ) representing Poisson noise are shown below each data spectrum. Interstellar lines discussed in the text are indicated. The location of a redshifted Lyα line at 1258.126 Å ($z = 0.03492$) with $W_\lambda \approx 220$ mÅ is also indicated.

Fig. 2. – A portion of the far-ultraviolet spectrum of ESO 141-055 observed with the Berkeley spectrograph on the ORFEUS-II mission. The data, which have been binned into 0.1 Å samples, have S/N ≈ 7 per 0.3 Å (100 $\mathrm{km\,s^{-1}}$) resolution element. Airglow features have been removed. The dashed line is a 1σ error vector. Data below 1000 Å are not shown since the S/N is very low (<3 per resolution element).

Fig. 3. – Normalized absorption profiles of the high ionization lines toward ESO 141-055 observed with the GHRS (Si IV, C IV, N V) and ORFEUS-II (O VI). The Si II λ1260.42 line includes blended Fe II λ1260.53 absorption near +26 $\mathrm{km\,s^{-1}}$. The O VI λ1037.62 absorption is blended with absorption by C II λ1036.34, (–370 $\mathrm{km\,s^{-1}}$), C II* λ1037.02 (–173 $\mathrm{km\,s^{-1}}$), and the 5–0 R(1) and P(1) lines of H_2 near 1037.15 Å (–135 $\mathrm{km\,s^{-1}}$) and 1038.16 Å (+157 $\mathrm{km\,s^{-1}}$). The O VI λ1031.93 absorption is blended with the H_2 (6–0) P(3) line at 1031.19 Å (–214 $\mathrm{km\,s^{-1}}$). Several Si II and S II lines observed with the GHRS are shown in the right panel for comparison with the high ion lines.

Fig. 4. – *Top Panel*: H I 21 cm emission profile composite from Colomb et al. (1980) for $|v_{\mathrm{LSR}}| \leq 50$ $\mathrm{km\,s^{-1}}$ ($\Delta v = 2$ $\mathrm{km\,s^{-1}}$, beamwidth (HPBW) = 30′) and from Cleary et al. (1979) for $|v_{\mathrm{LSR}}| \geq 50$ $\mathrm{km\,s^{-1}}$ ($\Delta v = 7$ $\mathrm{km\,s^{-1}}$, beamwidth (HPBW) = 48′). *Lower Panels*: Apparent column density profiles for the S II, Si IV, C IV, and N V lines observed with the GHRS. The histograms are the profiles for the weaker member of each doublet/multiplet, and the filled points are the profiles for the stronger member. Systematic underestimates of $N_a(v)$ by the stronger lines at some velocities (typically, the line cores) indicate that modest saturation corrections are necessary to recapture the total column densities of S II, Si IV, and C IV (see text). Typical errors associated with the individual values of $N_a(v)$ are shown as vertical error bars at the right of each panel.

Fig. 5. – Enlarged view of the 1000–1100 Å spectral region of the ESO 141-055 ORFEUS-II data shown in Figure 2. The data is shown as a histogrammed spectrum. The solid smooth curve is the absorption spectrum predicted by the neutral cloud model described in §3.2. Molecular hydrogen and atomic features arising in the H I gas are labeled. (The H_2 lines are indicated by their rotational and vibrational levels.) The model cloud has $\log N(\mathrm{H\ I}) = 20.54$, $\log N(H_2) = 19.00$, and a solar mix of heavy elements. Atomic features due to Ar I and Fe II that are not seen or are weaker than the model predictions are

indicated under the spectrum with asterisks. Absorption features due to ionized gas (e.g., O VI λ1031.93 and N II λ1083.99) are present in the spectrum. There is an unidentified feature at 1041.2 Å.

Fig. 6. – *Left panels*: C IV apparent column density profiles for the ESO 141-055 sight line and the sight lines to four stars located in the inner regions of the Galaxy. The Galactic coordinates and distances of each object are indicated under the object name. The $N_a(v)$ profiles for the stellar sight lines are from IUE or GHRS data presented in previous work cited in §4.2. *Right panels*: These three panels contain the Galactic rotation curve and predicted apparent column density profiles for the ESO 141-055 sight line assuming a smooth exponential gas distribution away from the Galactic plane. The rotation curve is from Clemens (1985); the horizontal ticks on this curve indicate the |z|-distance of the sight line (in kpc) at a given velocity. The model column density profiles are normalized to their peak values and are appropriate for cases in which either the velocity dispersion (σ) or vertical scale height (h_z) of the gas is allowed to vary. The three values of the parameter being varied (σ or h_z) are shown as solid, dashed, and dotted curves as identified in the panel legends. The models assume that gas at all distances from the Galactic plane obeys the rotation curve shown in the top panel.

Fig. 7. – Galactic locations of the sight lines for which $N_a(v)$ profiles are shown in Figure 6. "GC" indicates the location of the Galactic center.

Fig. 8. – A 7.5° × 7.5° IRAS 100μm map of the region of sky surrounding the ESO 141-055 sight line (rectangluar equatorial coordinate projection). North is toward the top and east is to the left. The location of the sight line is indicated by an asterisk. These IRAS Sky Survey Atlas data have a spatial resolution of $\sim$2′. The solid lines indicate 100μm contour levels of 4, 8, and 12 MJy sr^{-1}.

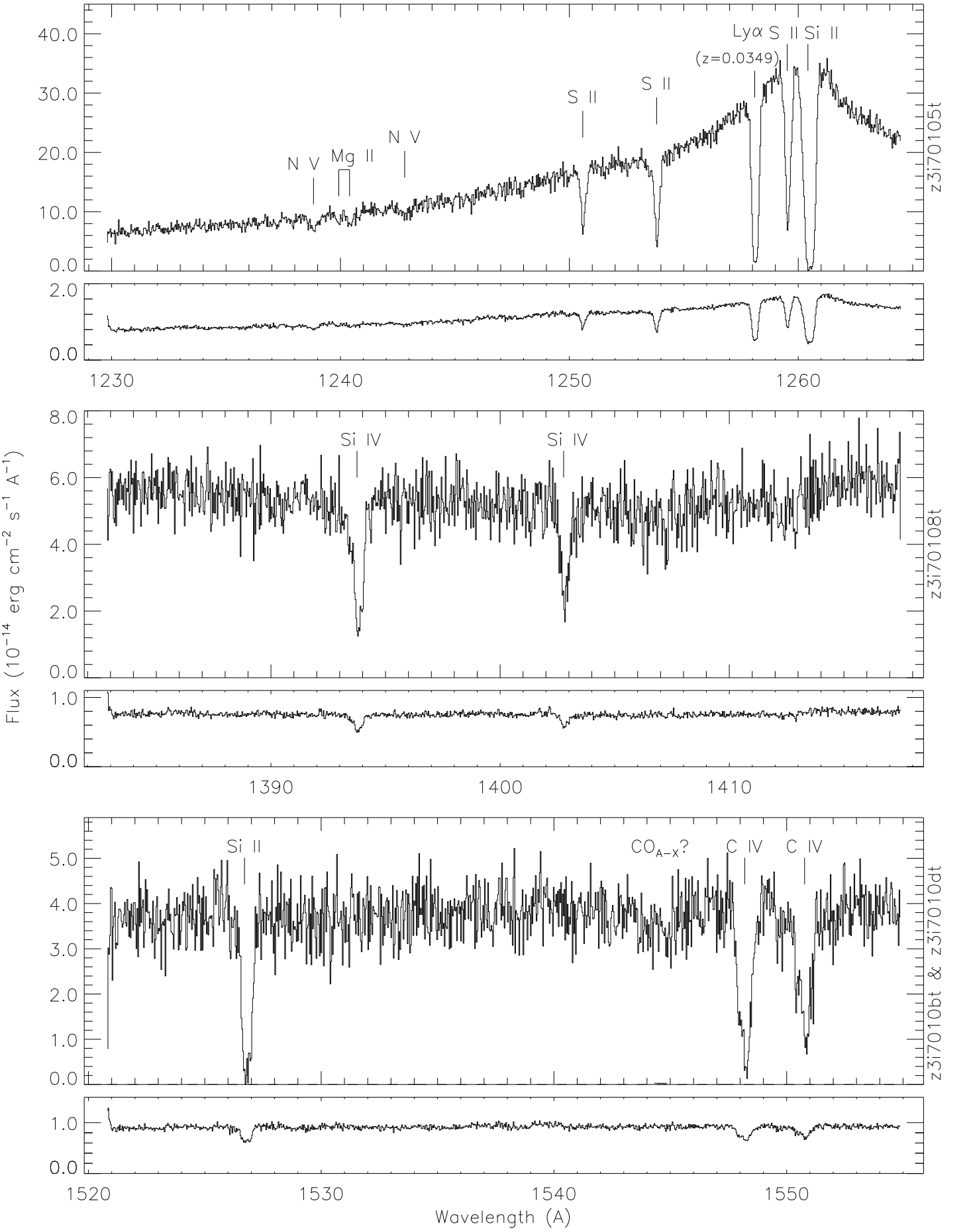
Lyα
S II
Si II
(z=0.0349)
S II
S II
N V
Mg II
N V
z3i7010 5t
Si IV
Si IV
z3i7010 8t
Si II
CO A-X ?
C IV
C IV
z3i7010 10bt & z3i7010 10dt
Flux (10^-14 erg cm^-2 s^-1 A^-1)
Wavelength (A)

Figure 1

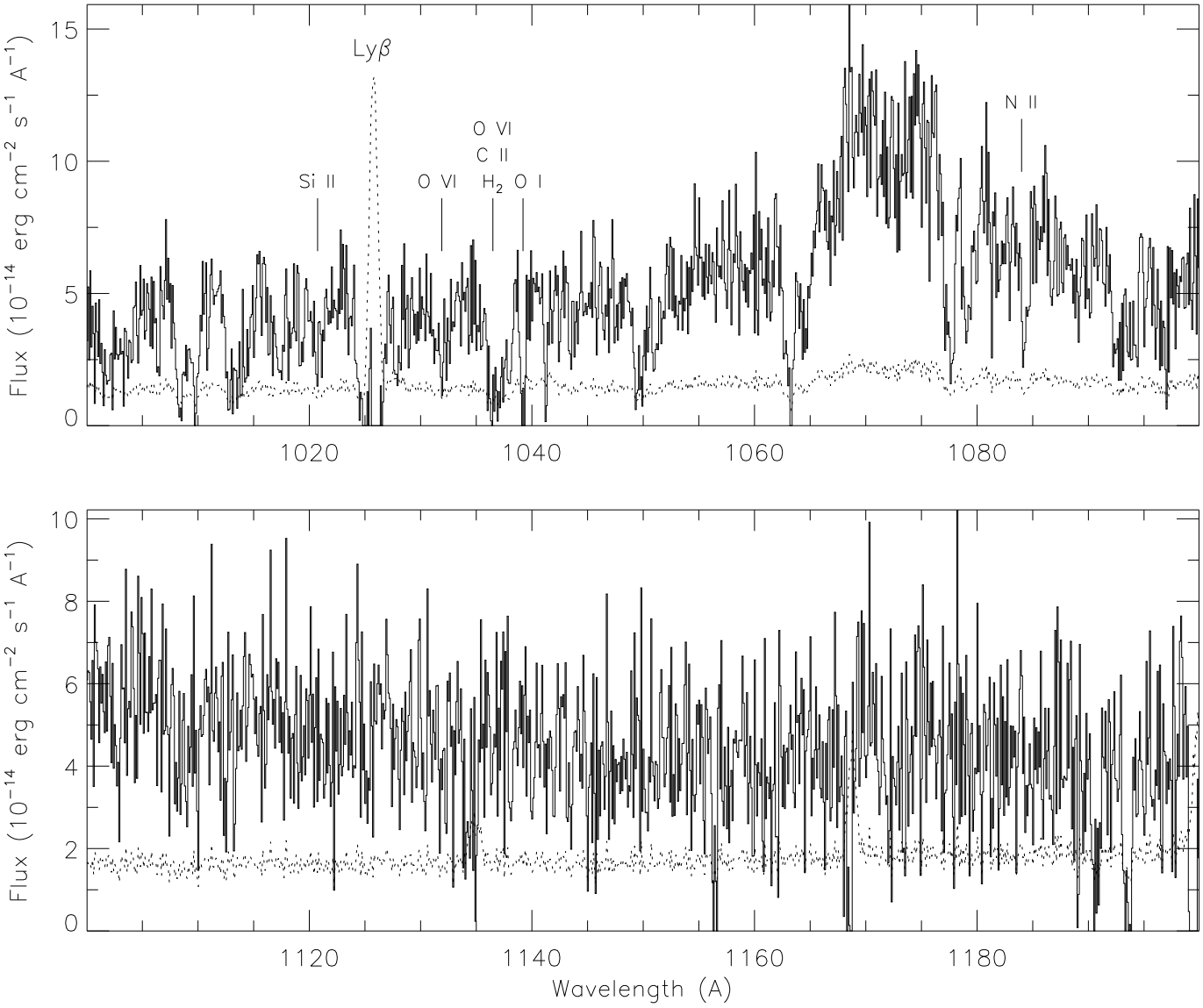
Flux (10^{-14} erg cm^{-2} s^{-1} A^{-1})
Lyβ
Si II
O VI
O VI
C II
H_2
O I
N II
Wavelength (A)

Figure 2

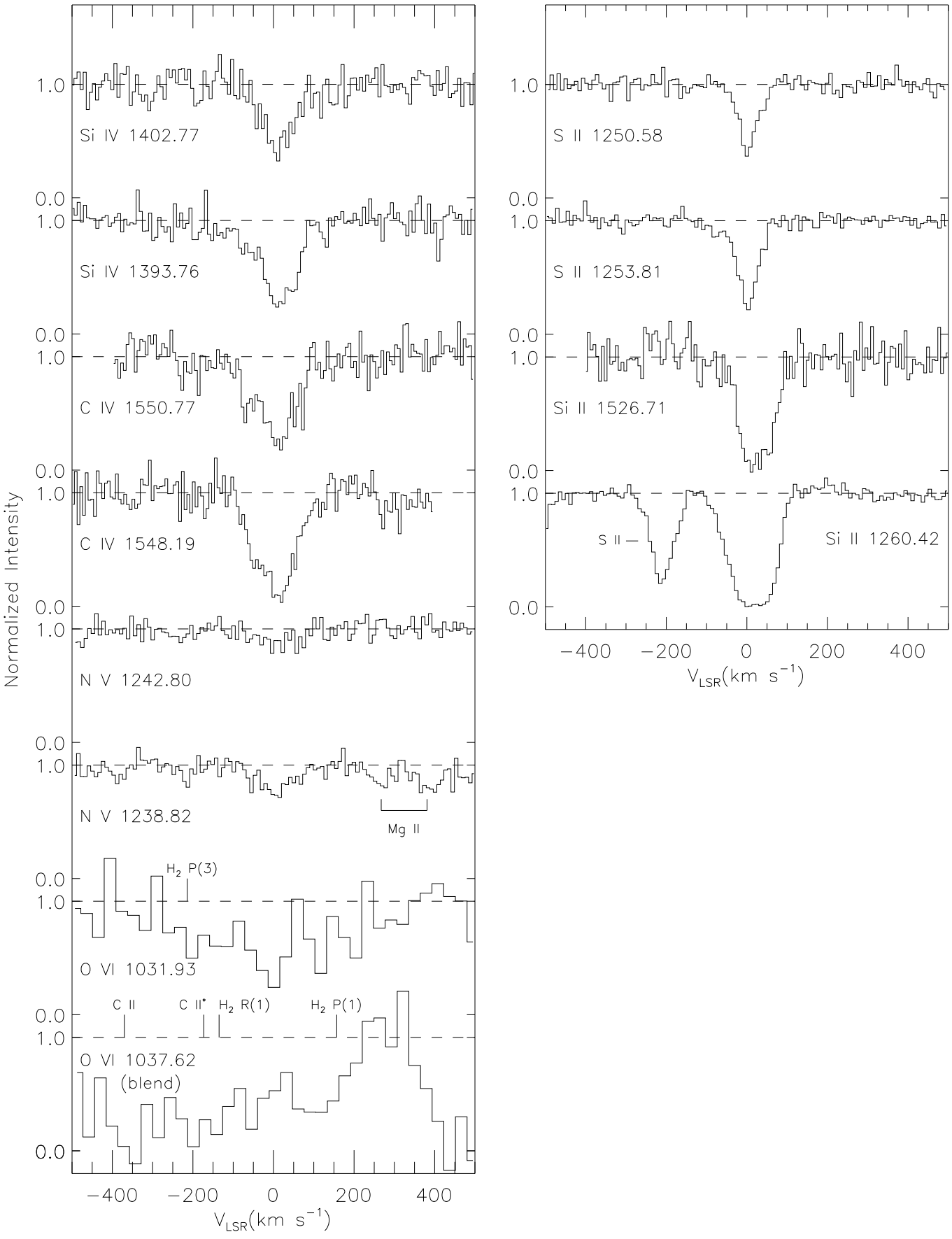
Normalized Intensity
Si IV 1402.77
Si IV 1393.76
C IV 1550.77
C IV 1548.19
N V 1242.80
N V 1238.82
Mg II
H2 P(3)
O VI 1031.93
C II
C II*
H2 R(1)
H2 P(1)
O VI 1037.62
(blend)
S II 1250.58
S II 1253.81
Si II 1526.71
S II
Si II 1260.42
VLSR(km s−1)

Figure 3

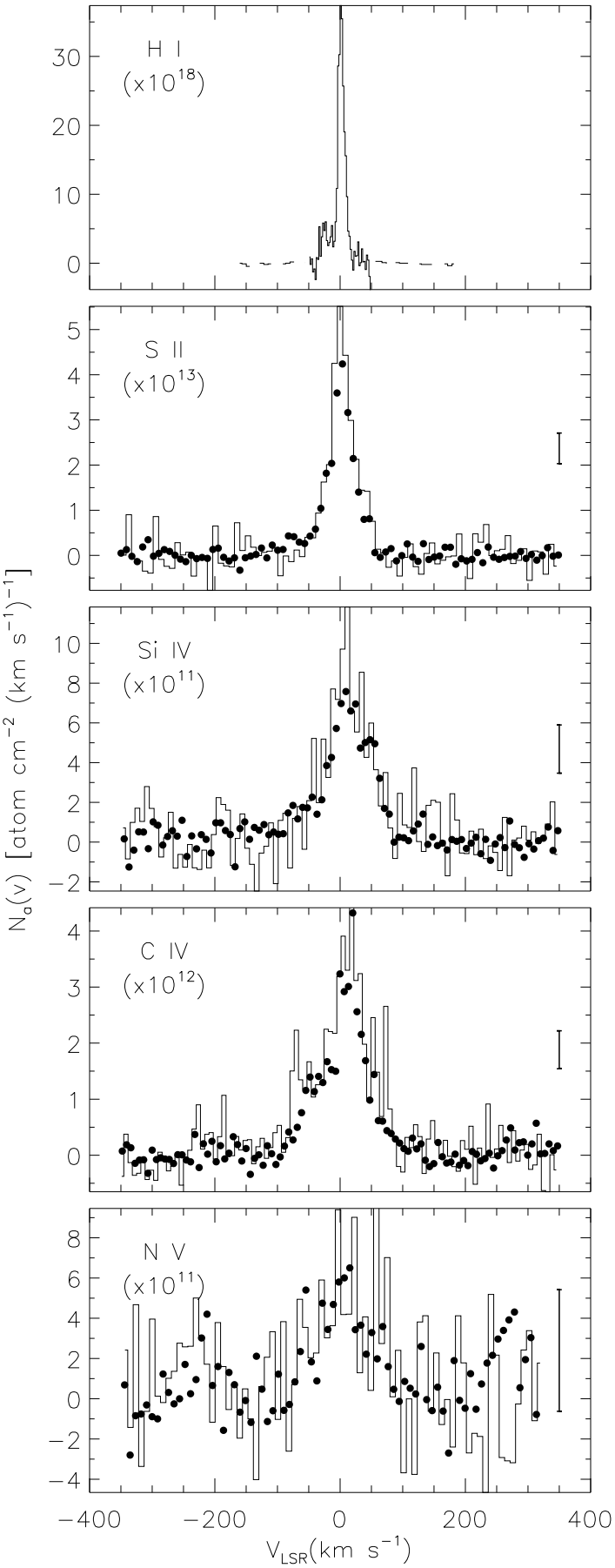
H I
(x10^18)
S II
(x10^13)
Si IV
(x10^11)
C IV
(x10^12)
N V
(x10^11)
N_a(v) [atom cm^-2 (km s^-1)^-1]
V_LSR(km s^-1)

Figure 4

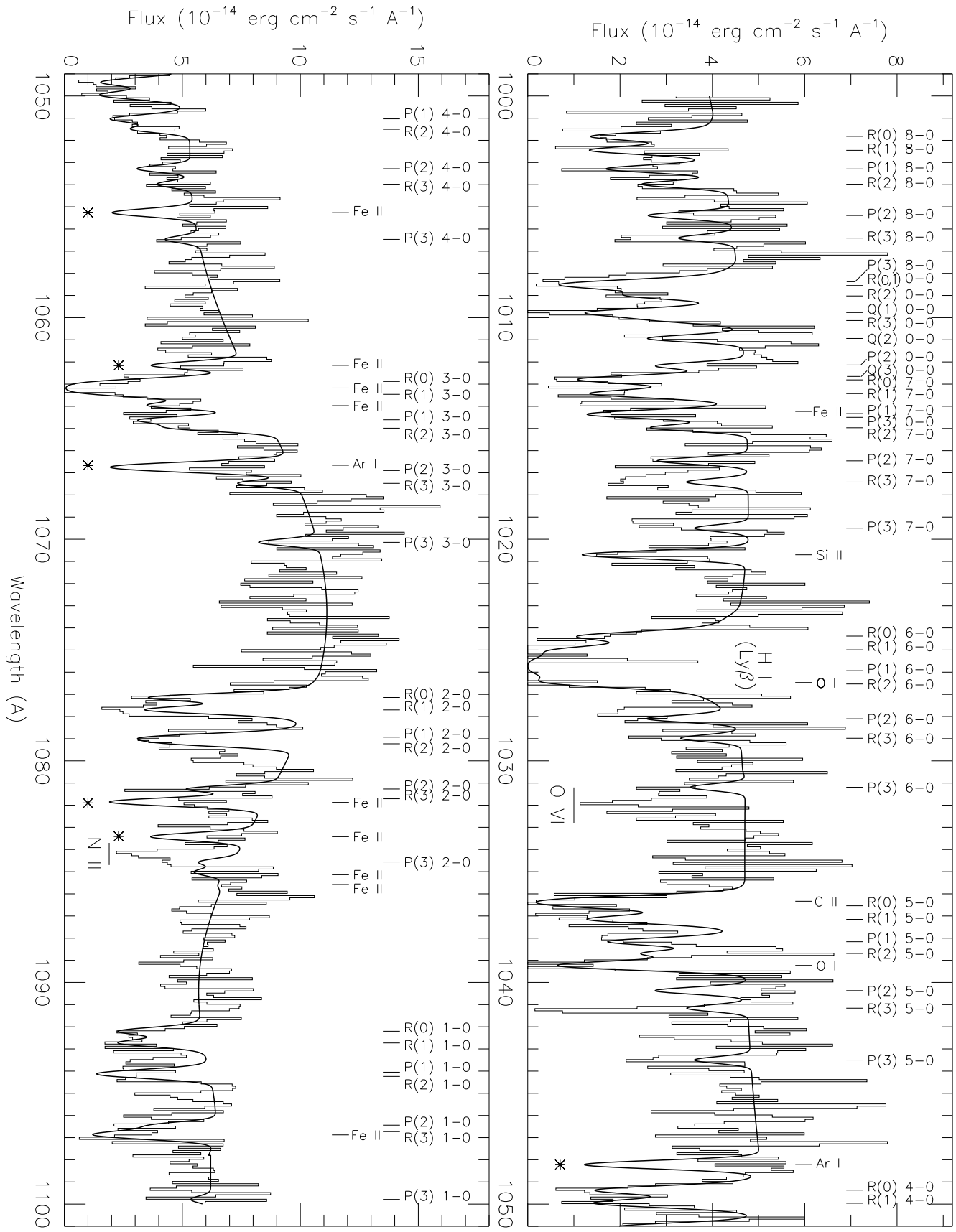
Flux (10^{-14} erg cm^{-2} s^{-1} A^{-1})
Wavelength (A)
P(1) 4-0
R(2) 4-0
P(2) 4-0
R(3) 4-0
Fe II
P(3) 4-0
Fe II
R(0) 3-0
Fe II
R(1) 3-0
Fe II
P(1) 3-0
R(2) 3-0
Ar I
P(2) 3-0
R(3) 3-0
P(3) 3-0
R(0) 2-0
R(1) 2-0
P(1) 2-0
R(2) 2-0
P(2) 2-0
R(3) 2-0
Fe II
N II
Fe II
P(3) 2-0
Fe II
Fe II
R(0) 1-0
R(1) 1-0
P(1) 1-0
R(2) 1-0
P(2) 1-0
Fe II
R(3) 1-0
P(3) 1-0
R(0) 8-0
R(1) 8-0
P(1) 8-0
R(2) 8-0
P(2) 8-0
R(3) 8-0
P(3) 8-0
R(0) 0-0
R(2) 0-0
Q(1) 0-0
R(3) 0-0
Q(2) 0-0
P(2) 0-0
Q(3) 0-0
R(0) 7-0
R(1) 7-0
Fe II
P(1) 7-0
P(3) 0-0
R(2) 7-0
P(2) 7-0
R(3) 7-0
P(3) 7-0
Si II
H I (Lyβ)
O I
R(0) 6-0
R(1) 6-0
P(1) 6-0
R(2) 6-0
P(2) 6-0
R(3) 6-0
P(3) 6-0
O VI
C II
R(0) 5-0
R(1) 5-0
P(1) 5-0
R(2) 5-0
O I
P(2) 5-0
R(3) 5-0
P(3) 5-0
Ar I
R(0) 4-0
R(1) 4-0

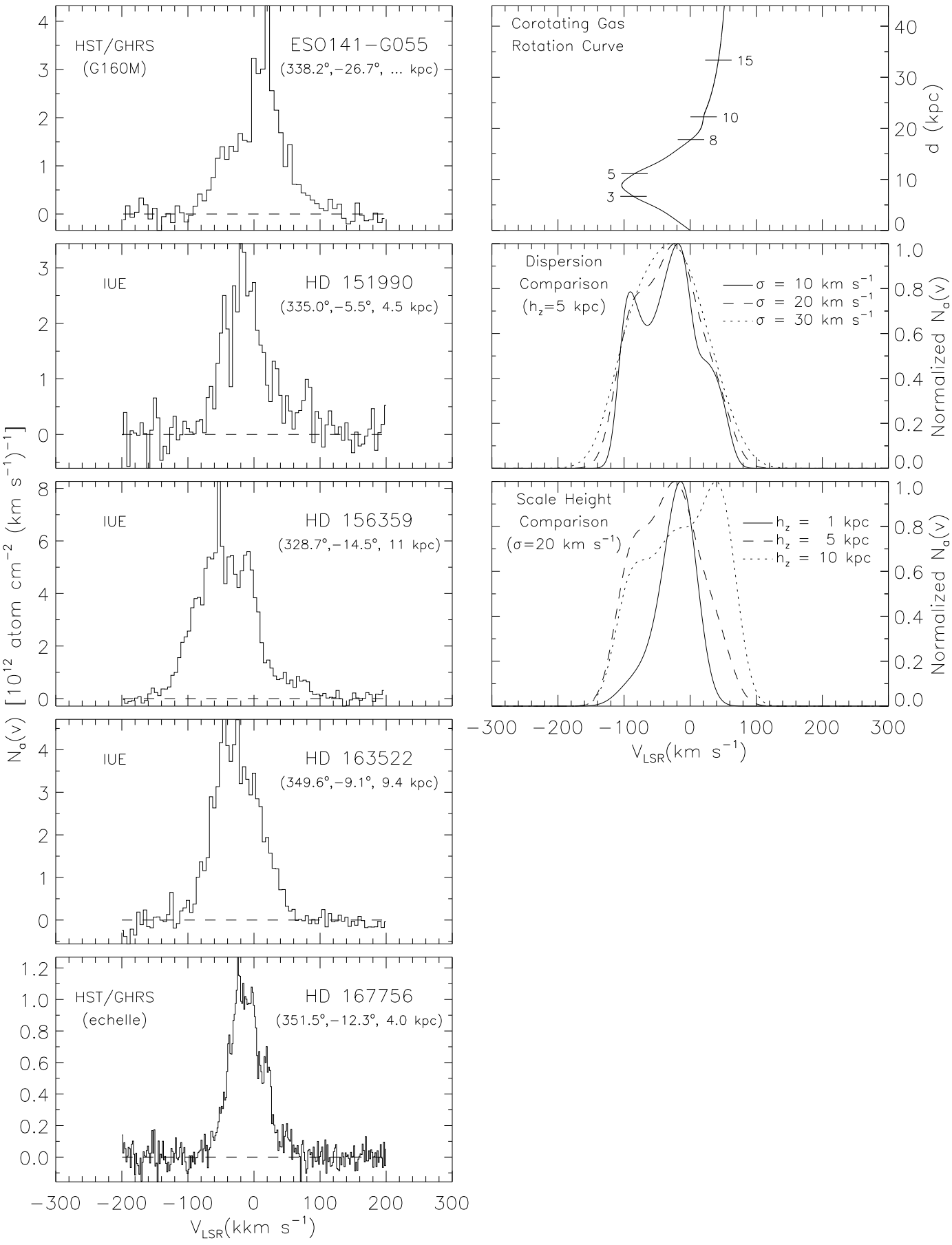
HST/GHRS
(G160M)
ESO141−G055
(338.2°,−26.7°, ... kpc)
IUE
HD 151990
(335.0°,−5.5°, 4.5 kpc)
IUE
HD 156359
(328.7°,−14.5°, 11 kpc)
IUE
HD 163522
(349.6°,−9.1°, 9.4 kpc)
HST/GHRS
(echelle)
HD 167756
(351.5°,−12.3°, 4.0 kpc)
N_a(v) [10^12 atom cm^-2 (km s^-1)^-1]
V_LSR(kkm s^-1)
Corotating Gas
Rotation Curve
15
10
8
5
3
d (kpc)
Dispersion
Comparison
(h_z=5 kpc)
σ = 10 km s^-1
σ = 20 km s^-1
σ = 30 km s^-1
Scale Height
Comparison
(σ=20 km s^-1)
h_z = 1 kpc
h_z = 5 kpc
h_z = 10 kpc
Normalized N_a(v)
V_LSR(km s^-1)

Figure 6

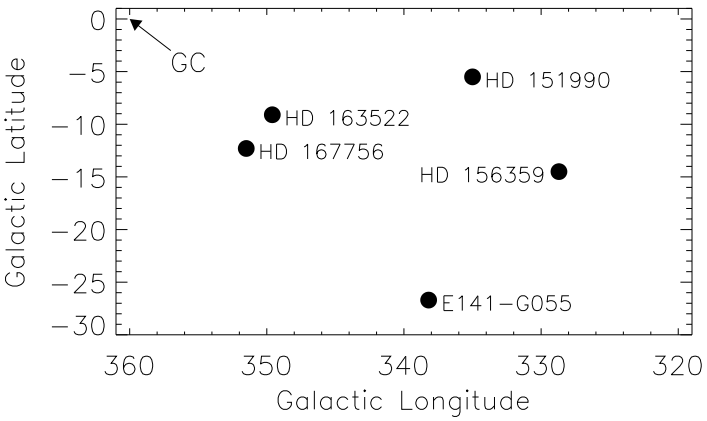
0
−5
−10
−15
−20
−25
−30
Galactic Latitude
GC
HD 151990
HD 163522
HD 167756
HD 156359
E141−G055
360
350
340
330
320
Galactic Longitude

Figure 7

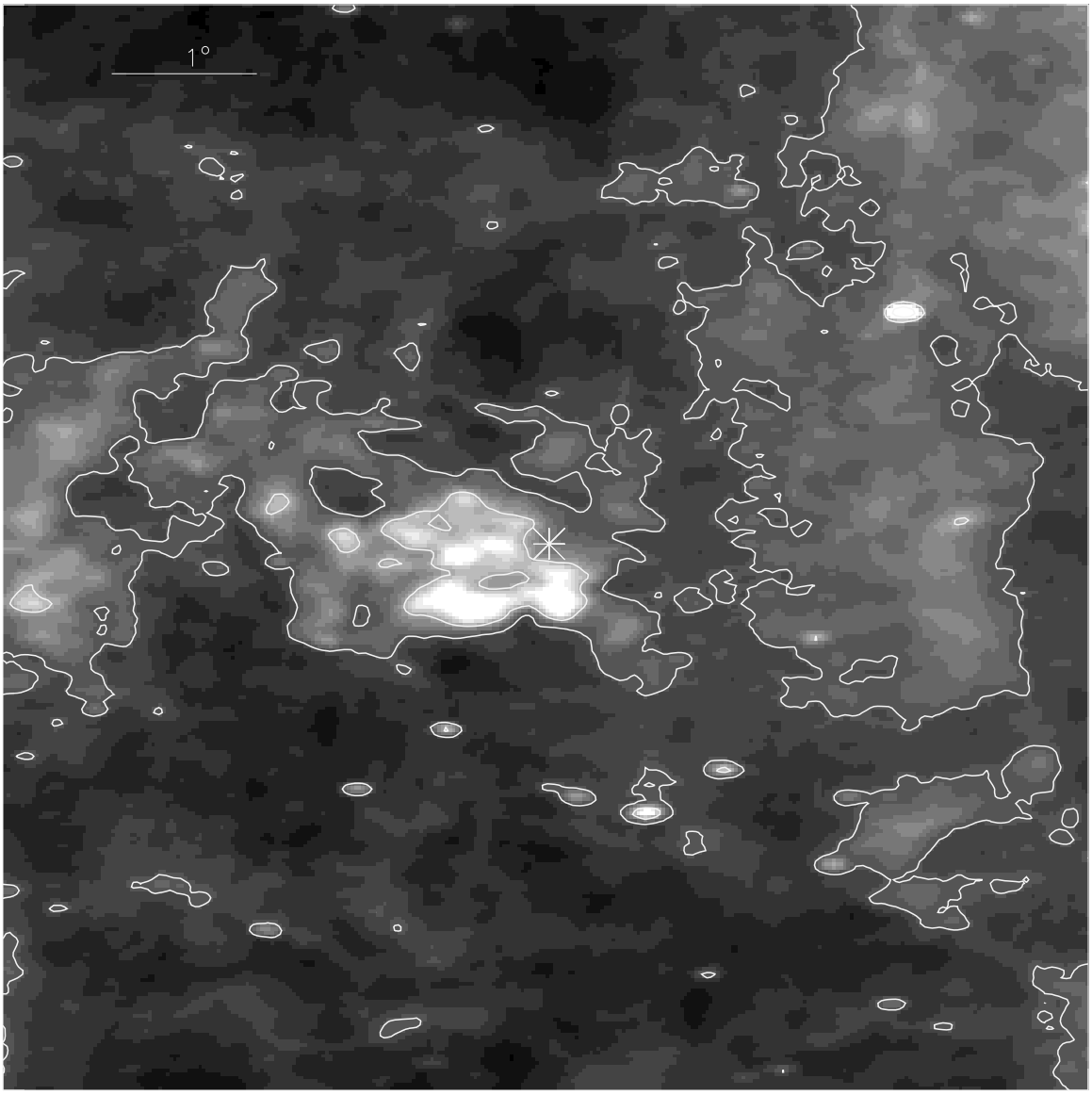

Figure 8

arXiv:astro-ph/9905343v1 26 May 1999

TABLE 1
EQUIVALENT WIDTHS AND COLUMN DENSITIES[a]

Ion	λ (mÅ)	f	$v_{min,max}$ ($\mathrm{km\,s^{-1}}$)	$< v_{LSR} >$ ($\mathrm{km\,s^{-1}}$)	FWHM ($\mathrm{km\,s^{-1}}$)	W_λ (mÅ)	Log N_a ($\mathrm{cm^{-2}}$)	Log N ($\mathrm{cm^{-2}}$)
				High Ions				
Si IV	1402.770	0.2553	−130, +140	+12	92	262±24	13.90±0.04	13.96±0.06
	1393.755	0.5140	−130, +140	+13	110	409±22	13.84±0.04	$(13.89\pm^{0.12}_{0.09})$
C IV	1550.770	0.0952	−130, +140	+4	127	481±28	14.56±0.04	14.74±0.10
	1548.195	0.1908	−130, +140	+5	122	560±25	14.42±0.03	$(14.90\pm^{0.71}_{0.20})$
N V	1242.804	0.0782	−130, +140	+5	140	72±20	$13.87\pm^{0.10}_{0.14}$	13.82±0.10
	1238.821	0.1570	−130, +140	+4	137	112±17	$13.77\pm^{0.07}_{0.08}$	$(13.96\pm^{0.61}_{0.23})$
O VI	1031.926	0.1329	−150, +100	−20:	202:	537±100	>14.7	15.0±0.3[b]
	1037.617	0.0661	...	...	...	blend	...	
				Low Ions				
Si II	1526.707	0.1270[d]	−130, +130	+20	100	531±25	>14.30	>14.30
	1260.422	1.1150[e]	−130, +130	+15	130	>568[c]	···	···
S I	1401.514	0.0149[f]	−100, +90	···	···	<32	<14.09	<14.09
S II	1250.584	0.0054	−100, +90	+3	45	135±13	15.38±0.05	15.45±0.06
	1253.811	0.0109	−100, +90	+3	45	212±10	15.31±0.03	$(15.39\pm^{0.11}_{0.09})$
	1259.519	0.0162	−100, +90	...	...	>221[c]	>15.20[c]	···

[a]The entries in this table include the ion observed, vacuum wavelength from Morton (1991), f-value from Morton (1991) unless otherwise specified, approximate velocity range, average velocity, full width at half maximum intensity, equivalent width, integrated apparent column density, and adopted column density based on the values of N_a as described in the text. The numbers in parentheses in the final column are single-component Doppler-broadened curve-of-growth estimates based on the listed equivalent widths. The associated b-values are b(Si IV) = $48\pm^{30}_{12}$ $\mathrm{km\,s^{-1}}$, b(C IV) = $32\pm^{6}_{8}$ $\mathrm{km\,s^{-1}}$, b(N V) = $14\pm^{\cdot}_{7}$ $\mathrm{km\,s^{-1}}$, and b(S II) = $27\pm^{14}_{7}$ $\mathrm{km\,s^{-1}}$. All errors are 1σ estimates. All limits are 2σ estimates.

[b]This O VI column density was derived from the listed equivalent width, assuming a single component Doppler-broadened curve-of-growth with a b-value of 57±8 $\mathrm{km\,s^{-1}}$, as determined by fitting a single Gaussian component to the N V λ1238.82 line.

[c]Interstellar Si II λ1260.42 and S II λ1259.52 occur near the peak of the Lyα emission of ESO 141-055. The ESO 141-055 continuum curvature is uncertain at these wavelengths, and therefore the listed values of W_λ and N_a for these lines should be considered lower limits.

[d]f-value from Schectman et al. (1998).

[e]f-value from Dufton et al. (1983).

[f]f-value from Federman & Cardelli (1985).

TABLE 2

PROJECTED COLUMN DENSITIES (LOG $N \sin|b|$) FOR THE HIGH IONS

	ESO 141-055 (b = –26.7°)	HD 36402 (LMC)[a] (b = –33.0°)	PKS 2155-304[b] (b = –52.2°)	3C 273[c] (b = +64.4°)	Galactic Average[d]
Si IV	13.61±0.06	13.30±0.14	···	13.74±0.04	$13.56\pm^{0.07}_{0.08}$
C IV	14.39±0.10	13.90±0.03	14.01±0.04	14.45±0.03	$14.08\pm^{0.07}_{0.08}$
N V	13.47±0.10	···	13.62±0.13	13.83±0.06	$13.40\pm^{0.09}_{0.12}$
O VI	14.65±0.30	$14.51\pm^{0.15}_{0.24}$	<14.23	$14.80\pm^{0.11}_{0.15}$	(*14.59*)

[a]Values for HD 36402 are from Sembach & Savage (1992) and Widmann et al. (1998).

[b]Values for PKS 2155-304 are from Savage et al. (1997) and Hurwitz et al. (1995).

[c]Values for 3C 273 are from Sembach et al. (1997) and Hurwitz et al. (1998b).

[d]These Galactic averages for Si IV, C IV, and N V (Savage et al. 1997) are based upon 8–12 AGN/QSO sight lines and ∼30 sight lines toward OB stars in the Galactic disk and low halo. The O VI value is an average for the four sight lines listed, with the upper limit for PKS 2155-304 treated as a detection.

TABLE 3
COMPARISON OF OBSERVED IONIC RATIOS TO THEORY

Ratio	Observed[a]			<Disk-Halo>[b]	Mixing	Cooling	Conductive
	ESO 141-055	PKS 2155-304	3C 273		Layers[c]	Fountain[d]	Interface[e]
N(C IV)/N(Si IV)	6.0±1.5	···	4.8±0.5	5.1±0.6	1.6–4.5	3.0–4.7	20–26
N(C IV)/N(N V)	8.3±2.4	2.5±0.7	4.0±0.6	4.2±0.6	9.1–28	2.2–6.8	1.8–2.6
N(C IV)/N(O VI)	0.55±0.30	<0.6	0.44±0.13	$^{0.1-0.3\ Disk}_{0.3-1.7\ Halo}$	1.2–3.4	0.1–0.5	0.2–0.4

[a]Observed ionic ratios for ESO 141-055 (this paper), PKS 2155-304 (Hurwitz et al. 1995; Savage et al. 1997), and 3C 273 (Sembach et al. 1997; Hurwitz et al. 1998b).

[b]Average disk and halo sight line ratios from Sembach et al. (1997) for N(C IV)/N(Si IV) and N(C IV)/N(N V). The ranges for N(C IV)/N(O VI) are from Spitzer (1996).

[c]Turbulent mixing layer ratios from Slavin et al. (1993) for a post-mixed gas temperature of 3×10^5 K, solar abundances, and an entrainment velocity of 25–100 $\mathrm{km\,s^{-1}}$.

[d]Radiative cooling ratios for a gas heated to $\sim10^6$ K and allowed to cool with self-photoionization within the flow included (Benjamin & Shapiro 1999).

[e]Magnetized conductive interface ratios from Borkowski et al. (1990) for a front with an age of 2.5×10^5 years and magnetic field inclinations between 60°–0° relative to the front normal direction.